Dynamics and Deposits of Pyroclastic Density Currents in Magmatic and Phreatomagmatic Eruptions Revealed by a Two-Layer Depth-Averaged Model

Hiroyuki A. Shimizu[1], Takehiro Koyaguchi[2], and Yujiro J Suzuki[2]

[1]Sabo & Landslide Technical Center
[2]University of Tokyo

June 8, 2023

Abstract

A pyroclastic density current (PDC) is characterized by its strong stratification of particle concentration; it consists of upper dilute and lower dense currents, which control the dynamics and deposits of PDCs, respectively. To explain the relationship between the dynamics and deposits for magmatic and phreatomagmatic eruptions in a unified way, we have developed a two-layer PDC model considering thermal energy conservation for mixing of magma, external water, and air. The results show that the run-out distance of dilute currents increases with the mass fraction of external water at the source (w_{mw}) owing to the suppression of thermal expansion of entrained air. For w_{mw}~0.07–0.38, the dense current is absent owing to the decrease in particle concentration in the dilute current, resulting in the direct formation of the deposits from the dilute current in the entire area. These results capture the diverse features of natural PDCs in magmatic and phreatomagmatic eruptions.

Hosted file

`SupportingMovie1.mov` available at https://authorea.com/users/624693/articles/646937-dynamics-and-deposits-of-pyroclastic-density-currents-in-magmatic-and-phreatomagmatic-eruptions-revealed-by-a-two-layer-depth-averaged-model

Hosted file

`SupportingMovie2.mov` available at https://authorea.com/users/624693/articles/646937-dynamics-and-deposits-of-pyroclastic-density-currents-in-magmatic-and-phreatomagmatic-eruptions-revealed-by-a-two-layer-depth-averaged-model

Dynamics and Deposits of Pyroclastic Density Currents in Magmatic and Phreatomagmatic Eruptions Revealed by a Two-Layer Depth-Averaged Model

Hiroyuki A. Shimizu[1,2], Takehiro Koyaguchi[3], and Yujiro J. Suzuki[3]

[1]Sabo & Landslide Technical Center, Tokyo, Japan.

[2]National Research Institute for Earth Science and Disaster Resilience, Ibaraki, Japan.

[3]Earthquake Research Institute, The University of Tokyo, Tokyo, Japan.

Corresponding author: Hiroyuki A. Shimizu (shimizu@stc.or.jp)

Key Points:

- A two-layer pyroclastic density current model with thermal energy conservation for mixing of magma, external water, and air is developed.
- In phreatomagmatic eruptions, the upper dilute current flows over longer distances and the lower dense current tends to be absent.
- Our results explain the diverse features of the dynamics and deposits of natural pyroclastic density currents in a unified way.

Abstract

A pyroclastic density current (PDC) is characterized by its strong stratification of particle concentration; it consists of upper dilute and lower dense currents, which control the dynamics and deposits of PDCs, respectively. To explain the relationship between the dynamics and deposits for magmatic and phreatomagmatic eruptions in a unified way, we have developed a two-layer PDC model considering thermal energy conservation for mixing of magma, external water, and air. The results show that the run-out distance of dilute currents increases with the mass fraction of external water at the source (w_{mw}) owing to the suppression of thermal expansion of entrained air. For $w_{\mathrm{mw}}{\sim}0.07-0.38$, the dense current is absent owing to the decrease in particle concentration in the dilute current, resulting in the direct formation of the deposits from the dilute current in the entire area. These results capture the diverse features of natural PDCs in magmatic and phreatomagmatic eruptions.

Plain Language Summary

Explosive volcanic eruptions eject a mixture of volcanic particles and gas (i.e., magma) from the vent and form eruption columns, which can collapse and propagate along the ground surface as a pyroclastic density current (PDC). The dynamics and deposits of PDCs are extremely diverse depending on the amount of external water (e.g., groundwater, lakes, and oceans) that mixes with magma. To explain the diverse features of the dynamics and deposits of PDCs for various amounts of external water, we have developed a two-layer model for stratified PDCs considering thermal energy conservation for mixing of magma and external water. The two-layer model successfully reproduces the dynamics and deposits of PDCs with strong stratification of particle concentrations in a unified way. The results show that the run-out distance of upper dilute currents increases with the increasing amount of external water. For a relatively small amount of external water, the lower dense current tends to be absent, resulting in the direct formation of the deposits from the dilute current in the entire area. These model predictions are useful to mitigate the diverse hazards caused by natural PDCs under various geological conditions.

1 Introduction

During explosive volcanic eruptions, a mixture of volcanic particles and gas ejected as an eruption column from the volcanic vent can collapse and propagate along the ground surface as a pyroclastic density current (PDC). The dynamical features of PDCs are highly variable because they are controlled by the eruption conditions, physical processes of PDCs (e.g., particle sedimentation, ambient air entrainment, and thermal expansion of entrained air), and topography (e.g., Dufek, 2016; Lube et al., 2020). These factors cause PDCs to form extremely diverse deposits (e.g., Fisher & Schmincke, 1984; Cas & Wright, 1987; Branney & Kokelaar, 2002; Sulpizio et al., 2014).

The effect of external water (e.g., groundwater, lakes, and oceans) on eruption styles (magmatic vs. phreatomagmatic eruptions) is a key factor leading to the diverse distribution and sedimentary structures of PDC deposits. Magmatic eruptions produce the PDC deposits with high temperatures of $\sim 700–1200$ K, whereas phreatomagmatic eruptions produce those with low temperatures of $\sim 300–700$ K (e.g., Koyaguchi & Woods, 1996; Trolese et al., 2017, 2019). The experimental and numerical simulations of PDCs (Ishimine, 2005; Andrews, 2014; Esposti Ongaro et al., 2016) suggested that the run-out distance of PDCs (i.e., the length of PDC deposits) increases as the source temperature decreases (i.e., the water:magma mass ratio increases). For phreatomagmatic eruptions, single PDC deposits can have spatial variation in sedimentary structures from poorly sorted massive facies to well sorted (cross-)stratified facies, as seen in base surge deposits (e.g., Wohletz & Sheridan, 1979). Understanding these diverse features of the dynamics and deposits of PDCs for magmatic and phreatomagmatic eruptions in a unified way is one major volcanological subject.

The relationship between the dynamics of PDCs and their deposits is not straightforward. The major difficulty comes from the fact that PDCs generally have strong stratification in terms of particle concentration (e.g., Branney & Kokelaar, 2002). Stratified PDCs comprise two main regions; an upper thick region of low particle volume fractions ($\lesssim 10^{-2}$) and a lower thin region of high particle volume fractions (~ 0.5). The upper dilute region behaves as a dilute turbulent suspension current that is controlled mainly by settling of particles, entrainment of ambient air, and thermal expansion of entrained air (e.g., Andrews & Manga, 2012). Through these physical processes, the dilute region partially becomes buoyant and lifts off the ground, which can control the run-out distance of the whole PDCs (e.g., Bursik & Woods, 1996; Dade & Huppert, 1996). On the other hand, the lower dense region behaves as a fluidized granular current that is controlled mainly by particle–particle and gas–particle interactions, frictional interaction between the current and the ground, and deposition at the base (e.g., Roche et al., 2010; Lube et al., 2019). The region directly affects the features of PDC deposits (e.g., sedimentary structure; Branney & Kokelaar, 2002).

To describe the global features of stratified PDCs and their deposits, numerical two-layer depth-averaged models have been developed (e.g., Doyle et al., 2008; Kelfoun, 2017; Shimizu et al., 2019). In the two-layer models, the continuous stratification of particle concentration and density in PDCs is modeled as upper and lower depth-averaged layers coupled through mass and momentum exchanges on the basis of the idea that the two regions in PDCs are controlled by different physical processes. This paper extends a two-layer model for large-scale PDCs in magmatic eruptions (Shimizu et al., 2019) to both magmatic and phreatomagmatic eruptions. The new model provides a theoretical framework for understanding the relationship between the diverse features of the dynamics and deposits of large-scale PDCs for magmatic and phreatomagmatic eruptions in a unified way.

2 Methods

We develop a two-layer model for large-scale PDCs in magmatic and phreatomagmatic eruptions by combining the two-layer PDC model of Shimizu et al. (2019) with a thermodynamical model for magmatic and phreatomagmatic eruptions (i.e., the thermal energy conservation for mixing of magma, external water, and ambient air in the collapsing eruption column; Koyaguchi & Woods, 1996). The model is designed to describe an axisymmetric PDC spreading from a collapsing column on a flat ground surface (Figure 1a). The source column consists of magma (i.e., volcanic particles and gas (water vapor)), external water, and air entrained into the column. It produces a radial dilute current from the column edge $r = r_0$ at a constant mass flow rate during time > 0, where r is the distance from the center of the column. Particles settling from the bottom of the dilute current can form a dense basal current (Figure 1b). The deposits progressively aggrade upward from the bottom of the dense or dilute current.

The source conditions of the dilute current are given as follows. Hot fragmented magma with temperature $T_{\mathrm{m}} = 1000$ K and water mass fraction $w_{\mathrm{m}} = 0.03$ mixes with cold external water with temperature $T_{\mathrm{w}} = 273$ K and is ejected from the vent; this study considers a wide range of mass fractions of external water in the mixture of magma and external water ($w_{\mathrm{mw}} = 0$– 0.6). The ejected material mixes with ambient air to form a collapsing column (air mass fraction at the column edge $n_{\mathrm{a0}} = 0.07$), which in turn forms a dilute current. The conservation of thermal energy between magma, external water, and air at atmospheric pressure gives the mass fractions of water vapor n_{v0} and liquid water n_{w0} and the temperature T_0 as a function of w_{mw} at $r = r_0$ (Figure 1c). As w_{mw} increases from 0 to ∼0.2, T_0 decreases from ∼950 to ∼373 K (100ºC), n_{v0} increases, and n_{w0} remains zero, because all the external water mixed with the magma vaporizes. When w_{mw} is larger than ∼0.2, T_0 hardly changes because T_0 is less than 100ºC and water vapor and liquid water coexist; n_{v0} decreases and n_{w0} increases as w_{mw} increases from ∼0.2. The other source conditions of the dilute current (i.e., the thickness h_0, velocity u_0, and column radius r_0) are obtained from the magma discharge rate ($\dot{M}_{\mathrm{m}} = 10^9\ \mathrm{kg\ s^{-1}}$), the Richardson number of the dilute current at $r = r_0$ ($Ri_0 = 1$), and the aspect ratio of h_0 to r_0 ($a_0 = 0.2$).

The basic equations of the two-layer PDC model developed by Shimizu et al. (2019) are extended by considering the presence of liquid water in the dilute current with low temperatures below 100ºC. To obtain the spatiotemporal variation of the mass fraction of liquid water in the dilute current, the condensation rate of water vapor and the resulting latent heat are considered in

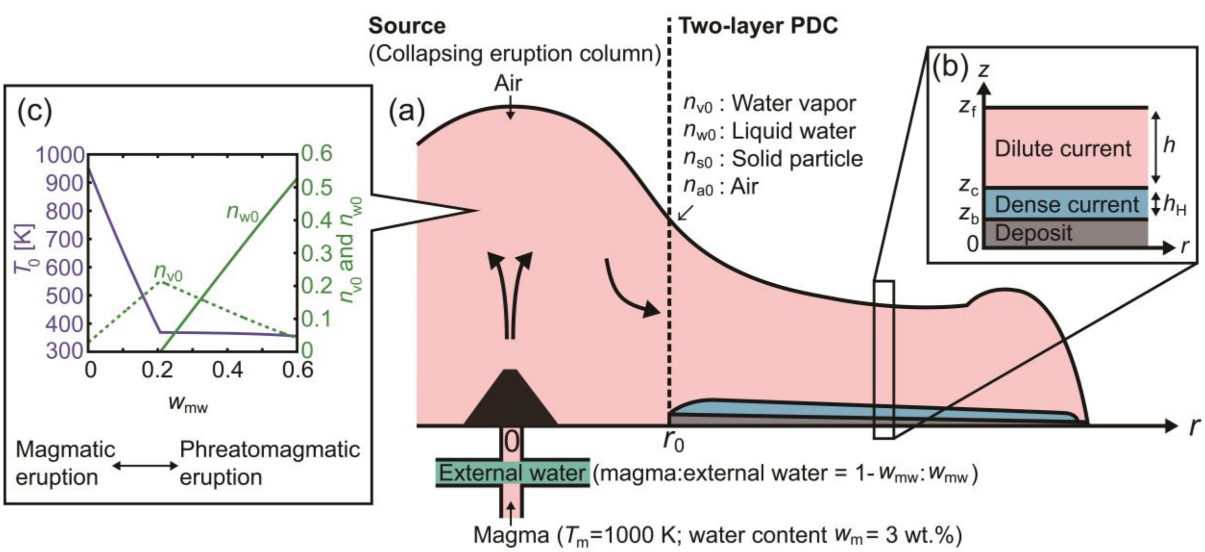

Figure 1. Illustration of the two-layer PDC model for magmatic and phreatomagmatic eruptions. (a) PDC spreading radially from the collapsing column edge $r = r_0$ over flat ground surface. (b) Dilute current (Red) forming a dense basal current (Blue). The deposit (Grey) progressively aggrades upward from the bottom of the dense (or dilute) current. (c) Source conditions at $r = r_0$ (i.e., temperature T_0 (purple line); mass fractions of water vapor n_{v0} (green dashed line) and liquid water n_{w0} (green solid line)) depending on the mass fraction of external water in the mixture of magma and external water w_{mw}.

the equation system on the basis of a moist eruption column model (Koyaguchi & Woods, 1996). Both the dynamics and deposits of two-layer PDCs are strongly controlled by the sedimentation process characterized by the settling speed of particles at the bottom of the dilute current (W_s) and the deposition speed at the bottom of the dense current (D); our representative simulations assume $W_\mathrm{s} = 0.5$ m s^{-1} and $D/W_\mathrm{s} = 1.22 \times 10^{-3}$. To investigate the effects of external water, we perform parametric study for $w_\mathrm{mw} = 0$– 0.6. We also assess the effects of the uncertainties of other parameters (i.e., w_m, T_m, n_a0, $\dot{M}_\mathrm{m}$, Ri_0, a_0, W_s, and D/W_s) on our conclusion. For details see Supporting Information S1–S3.

3 Results

Representative results for phreatomagmatic eruptions ($w_\mathrm{mw} = 0.3$) show that as a dilute current spreads radially from the column edge $r = r_0$ (Figure 2a and b; Supporting Movie S1), the mass density of the dilute current decreases through particle settling, air entrainment, and thermal expansion of entrained air. When the frontal region of the dilute current becomes lighter than the ambient air to lift off the ground (i.e., a co-ignimbrite ash plume forms), the front of the dilute current stops spreading and the dilute current converges to a steady state (Figure 2c), where the sum of the radial mass flux of particles from the front of the dilute current to the co-ignimbrite ash plume and the total particle settling rate at the bottom of the dilute current is balanced by the radial mass flux of particles from $r = r_0$. The particles settling from the bottom of the dilute current form the deposits.

The results for phreatomagmatic eruptions have the following two differences from typical results for magmatic eruptions ($w_\mathrm{mw} = 0$; Figure 2d–f; Supporting Movie S2). First, the lift-off of dilute currents with large w_mw is delayed (i.e., the run-out distance of dilute currents increases with w_mw; Red curve in Figure 3a). Secondly, for phreatomagmatic eruptions, the dense current can become absent (i.e., the run-out distance of dense currents decreases as w_mw increases from 0 to $\sim$0.07, it remains zero for $w_\mathrm{mw}\sim 0.07$– 0.38, and it increases as w_mw increases from $\sim$0.38; Blue curve in Figure 3a).

The increase in the run-out distance of dilute currents with w_{mw} is due to the suppression of thermal expansion of entrained air and the increase in the mass fraction of liquid water. The dilute-current density ρ is approximated as $p/((n_{\mathrm{a}}+n_{\mathrm{v}})RT)$, where p is the atmospheric pressure, n_{a} and n_{v} are the mass fractions of entrained air and water vapor, R is the gas constant

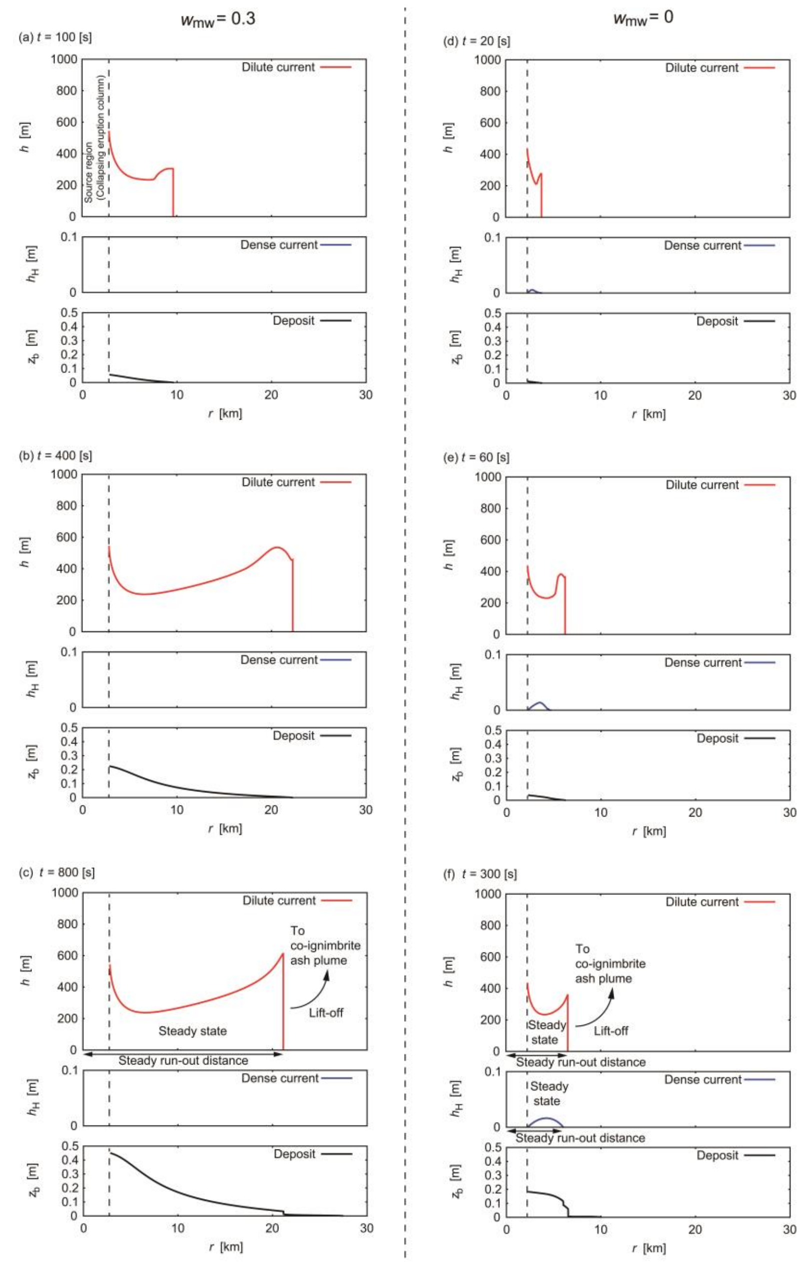

Figure 2. Representative numerical results of a two-layer PDC for phreatomagmatic eruption with $w_{\mathrm{mw}}=0.3$ at times $t=$ (a) 100, (b) 400, and (c) 800 s and those for magmatic eruption with $w_{\mathrm{mw}}=0$ at $t=$ (d) 20, (e) 60, and (f) 300 s. The thickness profiles of the dilute current ($h(r,t)$; red), dense current ($h_{\mathrm{H}}(r,t)$; blue), and deposits ($z_{\mathrm{b}}(r,t)$; black) are shown.

of the mixture of air and water vapor, and T is the dilute-current temperature. For large w_{mw} (low T), the dilute current entrains a large amount of air (has large n_{a}) before ρ becomes smaller than the ambient air density ρ_{a}; consequently, ρ/ρ_{a} is maintained above 1 over long distances (Figure 4a–c). Furthermore, as w_{mw} increases from ~ 0.2, the mass fraction of liquid water n_{w} increases (n_{v} decreases; Figure 1c), resulting in the increase in ρ/ρ_{a} and the delay of lift-off of dilute currents (Figure 4a–c). The delay of lift-off of dilute currents also leads to the decrease in proportions of co-ignimbrite ash-fall deposits with w_{mw} (Figure 3d).

The absence of any dense current for $w_{\mathrm{mw}} \sim 0.07 – 0.38$ (Grey region in Figure 3a) is explained by the balance of the particle settling rate at the bottom of the dilute current at $r = r_0$

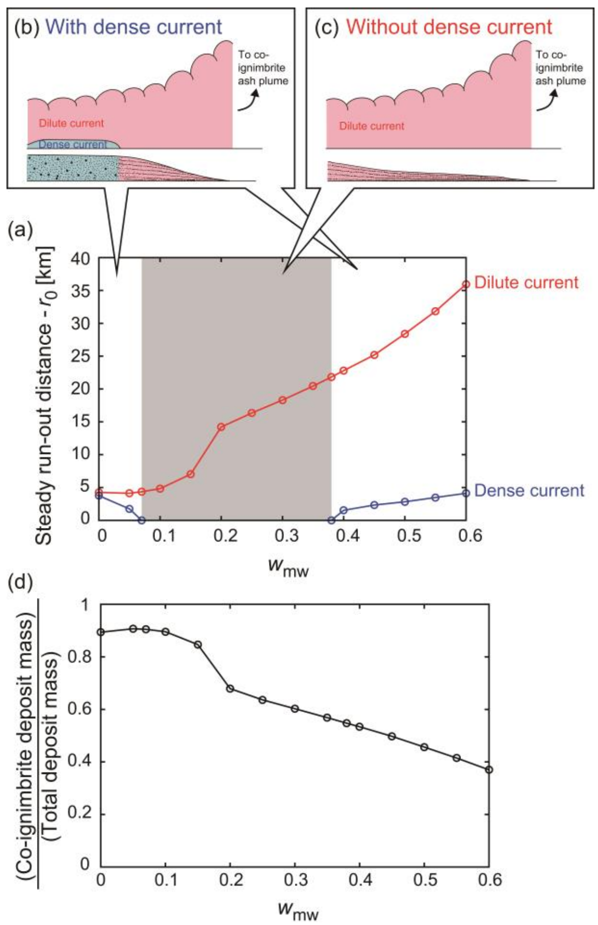

Figure 3. (a) Numerical results of the differences of the steady run-out distances of two-layer PDCs from the column radius r_0 as a function of mass fraction of external water w_{mw}. (b and c) Illustrations of two-layer PDCs and their deposits for (b) the case where the dense current is present and (c) the case where the dense current is absent. (d) Numerical results of the mass fraction of co-ignimbrite ash-fall deposits in the deposits of PDC and co-ignimbrite ash plume as a function of w_{mw}.

($\phi_{s0}W_s$) and the deposition rate at the bottom of the dense current ($\phi_{sD}D$) (i.e., $\phi_{s0}W_s < \phi_{sD}D$; Shimizu et al., 2019). In this balance, ϕ_{sD} and D/W_s are independent of w_{mw} (Black dashed line in Figure 4d). Therefore, the condition for the absence of dense currents depends on the solid volume fraction in the dilute current at $r = r_0$ (ϕ_{s0}); ϕ_{s0} decreases as w_{mw} increases from 0 to ~0.15 owing to the increase in n_{v0}, and it increases as w_{mw} increases from ~0.15 owing to the decrease in T_0 and the increase in n_{w0} (Figures 1c and 4d). In the range of $\phi_{s0} < \phi_{sD}D/W_s$ ($w_{mw} = 0.07$– 0.38), the dense current is absent throughout $r > r_0$. Our result is consistent with previous experimental and numerical studies (Lube et al., 2015; Breard et al., 2018; Valentine, 2020).

Although the above results are quantitatively affected by the uncertainties of parameters other than w_{mw}, they are not changed qualitatively (see Supporting Information S2).

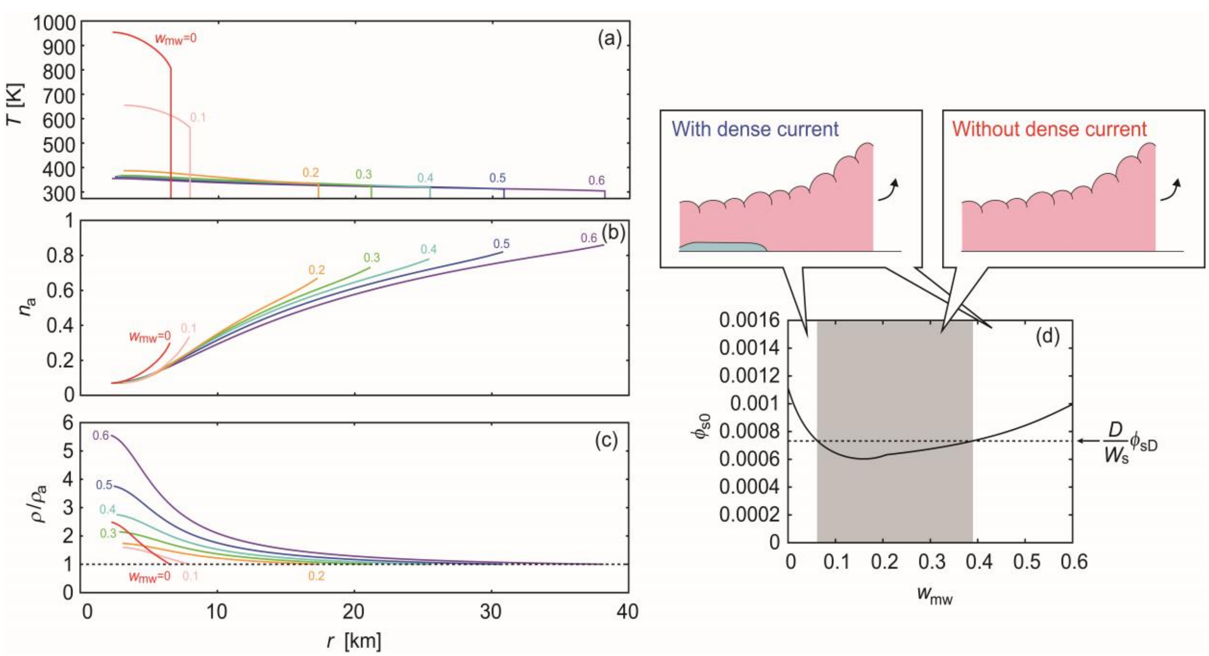

Figure 4. (a–c) Numerical results of steady-state two-layer PDCs with the mass fractions of external water $w_{mw} = 0$ (red), 0.1 (pink), 0.2 (orange), 0.3 (green), 0.4 (cyan), 0.5 (blue), and 0.6 (purple): (a) Temperature of dilute currents ($T(r,t)$); (b) Mass fraction of entrained air in dilute currents ($n_a(r,t)$); (c) Ratio of dilute-current density ($\rho(r,t)$) to ambient-air density (ρ_a). (d) Solid volume fraction in dilute currents at $r = r_0$ as a function of w_{mw} (ϕ_{s0}; solid curve), compared with $\phi_{sD}D/W_s$ (dashed line).

4 Geological Implications

We have obtained the two fundamental results: the run-out distance of dilute currents increases as w_{mw} increases (T_0 decreases); the dense current tends to be absent for intermediate values of w_{mw}. These results can provide a unified framework for understanding the diverse features of the dynamics and deposits of PDCs in magmatic and phreatomagmatic eruptions.

The results for cold dilute currents with large w_{mw} explain the low emplacement temperatures of PDC deposits for phreatomagmatic eruptions (e.g., Trolese et al., 2017, 2019). They also explain the long length of PDC deposits (i.e., the long run-out distance of PDCs) for phreatomagmatic eruptions. It is widely known that the run-out distance of PDCs correlates well with the magma discharge rate $\dot{M}_{\mathrm{m}}$ (e.g., Shimizu et al., 2019; Giordano & Cas, 2021; Roche et al., 2021). Roche et al. (2021) analyzed data from some large-scale PDCs to determine the relationships between the run-out distance and $\dot{M}_{\mathrm{m}}$ and showed that dilute PDCs over water in phreatomagmatic eruptions (the 161 ka Kos, 7234 BP Koya (unit C3), AD 1883 Krakatau, 2050 BP Okmok II, and Tosu – Aso 4II-1 PDCs) tend to have longer run-out distances than those on land in magmatic eruptions for a given $\dot{M}_{\mathrm{m}}$. This tendency can be explained by our results for large w_{mw}.

Our results for the presence and absence of dense currents explain diverse sedimentary structures in PDC deposits for magmatic and phreatomagmatic eruptions. The area where only the dilute current is present (the dense current is absent) becomes wider as w_{mw} increases (Figure 3a). The deposits in the area with the dense current are produced by deposition from the bottom of the dense current (Proximal area of Figure 3b), whereas the deposits in the area without the dense current are produced directly by particle settling from the bottom of the dilute current (Distal area of Figure 3b). Generally, the differences in the flow-particle interactions within the basal boundary layer between dilute and dense currents explain the wide variety of sedimentary structures in PDC deposits (Branney & Kokelaar, 2002). Deposition from the bottom of dilute currents forms (cross-)stratified facies (called "surge facies") through alternating series of tractional bedload transport and shifting sandwaves (Brosch & Lube, 2020) and deposition from the dense current forms massive, poorly sorted facies (called "flow facies") due to inhibited traction (Branney & Kokelaar, 2002). Thus, our results for large w_{mw} explain the observation that (cross-)stratified facies are widely produced in phreatomagmatic eruptions regardless of $\dot{M}_{\mathrm{m}}$ (Wohletz, 1998; Valentine & Fisher, 2000; De Rita et al., 2002). Furthermore, our results for the absence of dense currents for intermediate values of w_{mw} (Figure 3a and c) explain the fact that (cross-)stratified facies are more predominant in dry phreatomagmatic eruptions ($n_{\mathrm{w0}} = 0$) than in wet ones ($n_{\mathrm{w0}} > 0$) (Wohletz, 1998).

5 Conclusions

The present two-layer PDC model evaluates the effect of stratification of particle concentrations in PDCs and captures the diverse features of PDCs in magmatic and phreatomagmatic eruptions. The run-out distance of dilute currents for phreatomagmatic eruptions is longer than that for magmatic eruptions for a given magma discharge rate. For dry phreatomagmatic eruptions, the dense current tends to be absent and the dilute current directly forms deposits, explaining the variation of sedimentary structures commonly observed in PDC deposits. The model is expected to be a useful tool to analyze the dynamics and deposits for large-scale PDCs in magmatic and phreatomagmatic eruptions in a unified way.

Acknowledgments

This work was supported by MEXT KAKENHI Grant Number JP21K14018 and by MEXT's "Integrated Program for Next Generation Volcano Research and Human Resource Development."

Open Research

All data and post-processing scripts used to produce the figures of this paper are available in Zenodo (Shimizu, 2023; doi: 10.5281/zenodo.7928713).

References

Andrews, B. J. (2014). Dispersal and air entrainment in unconfined dilute pyroclastic density currents. *Bulletin of Volcanology*, *76*, 852, https://doi.org/10.1007/s00445-014-0852-4

Andrews, B. J., & Manga, M. (2012). Experimental study of turbulence, sedimentation, and coignimbrite mass partitioning in dilute pyroclastic density currents. *Journal of Volcanology and Geothermal Research*, *225–226*, 30–44. https://doi.org/10.1016/j.jvolgeores.2012.02.01

Branney, M. J., & Kokelaar, P. (2002). *Pyroclastic Density Currents and the Sedimentation of Ignimbrites* (Vol. 27, 150 p). Geological Society of London Memoir.

Breard, E. C. P., Dufek, J., & Lube, G. (2018). Enhanced mobility in concentrated pyroclastic density currents: An examination of a self-fluidization mechanism. *Geophysical Research Letters*, *45*, 654–664. https://doi.org/10.1002/2017GL075759

Brosch, E., & Lube, G. (2020). Spatiotemporal sediment transport and deposition processes in experimental dilute pyroclastic density currents. *Journal of Volcanology and Geothermal Research*, *401*, 106946. https://doi.org/10.1016/j.jvolgeores.2020.106946

Bursik, M. I., & Woods, A. W. (1996). The dynamics and thermodynamics of large ash flows. *Bulletin of Volcanology*, *58*, 175–193. https://doi.org/10.1007/s004450050134

Cas, R. A. F., & Wright, J. V. (1987). *Volcanic Successions: Modern and Ancient* (528 p). London, Allen and Unwin.

Dade, W. B., & Huppert, H. E. (1996). Emplacement of the Taupo ignimbrite by a dilute turbulent flow. *Nature*, *381*, 509–512. https://doi.org/10.1038/381509a0

De Rita, D., Giordano, G., Esposito, A., Fabbri, M., & Rodani, S. (2002). Large volume phreatomagmatic ignimbrites from the Colli Albani volcano (Middle Pleistocene, Italy). *Journal of Volcanology and Geothermal Research*, *118*, 77–98. https://doi.org/10.1016/S0377-0273(02)00251-2

Doyle, E. E., Hogg, A. J., Mader, H. M., & Sparks, R. S. J. (2008). Modeling dense pyroclastic basal flows from collapsing columns. *Geophysical Research Letters*, *35*, L04305. https://doi.org/10.1029/2007GL032585

Dufek, J. (2016). The fluid mechanics of pyroclastic density currents. *Annual Review of Fluid Mechanics*, *48*, 459–485. https://doi.org/10.1146/annurev-fluid-122414-034252

Esposti Ongaro, T., Orsucci, S., & Cornolti, F. (2016). A fast, calibrated model for pyroclastic density currents kinematics and hazard. *Journal of Volcanology and Geothermal Research*, *327*, 257–272. https://doi.org/10.1016/j.jvolgeores.2016.08.002

Fisher, R. V., & Schmincke, H.-U. (1984). *Pyroclastic Rocks* (427 p). Berlin, Springer.

Giordano, G., & Cas, R. A. F. (2021). Classification of ignimbrites and their eruptions. *Earth-Science Reviews*, *220*, 103697. https://doi.org/10.1016/j.earscirev.2021.103697

Ishimine, Y. (2005). Numerical study of pyroclastic surges. *Journal of Volcanology and Geothermal Research*, *139*, 33–57. https://doi.org/10.1016/j.jvolgeores.2004.06.017

Kelfoun, K. (2017). A two-layer depth-averaged model for both the dilute and the concentrated parts of pyroclastic currents. *Journal of Geophysical Research: Solid Earth*, *122*, 4293–4311. https://doi.org/10.1002/2017JB014013

Koyaguchi, T., & Woods, A. W. (1996). On the formation of eruption columns following explosive mixing of magma and surface-water. *Journal of Geophysical Research: Solid Earth*, *101*, 5561–5574. https://doi.org/10.1029/95JB01687

Lube, G., Breard, E. C. P., Cronin, S. J., & Jones, J. (2015). Synthesizing large-scale pyroclastic flows: Experimental design, scaling, and first results from PELE. *Journal of Geophysical Research: Solid Earth*, *120*, 1487–1502. https://doi.org/10.1002/2014JB011666

Lube, G., Breard, E. C. P., Jones, J., Fullard, L., Dufek, J., Cronin, S. J., & Wang, T. (2019). Generation of air lubrication within pyroclastic density currents. *Nature Geoscience*, *12*, 381–386. https://doi.org/10.1038/s41561-019-0338-2

Lube, G., Breard, E. C. P., Esposti-Ongaro, T., Dufek, J., & Brand, B. (2020). Multiphase flow behaviour and hazard prediction of pyroclastic density currents. *Nature Reviews Earth & Environment*, *1*, 348–365. https://doi.org/10.1038/s43017-020-0064-8

Roche, O., Montserrat, S., Niño, Y., & Tamburrino, A. (2010). Pore fluid pressure and internal kinematics of gravitational laboratory air-particle flows: Insights into the emplacement dynamics of pyroclastic flows. *Journal of Geophysical Research: Solid Earth*, *115*, B09206. https://doi.org/10.1029/2009JB007133

Roche, O., Azzaoui, N., & Guillin, A. (2021). Discharge rate of explosive volcanic eruption controls runout distance of pyroclastic density currents. *Earth and Planetary Science Letters*, *568*, 117017. https://doi.org/10.1016/j.epsl.2021.117017

Shimizu, H. A. (2023). Datasets for "Dynamics and deposits of pyroclastic density currents in magmatic and phreatomagmatic eruptions revealed by a two-layer depth-averaged model". https://doi.org/10.5281/zenodo.7928713

Shimizu, H. A., Koyaguchi, T., Suzuki, Y. J. (2019). The run-out distance of large-scale pyroclastic density currents: A two-layer depth-averaged model. *Journal of Volcanology* *and Geothermal Research*, *381*, 168–184. https://doi.org/10.1016/j.jvolgeores.2019.03.013

Sulpizio, R., Dellino, P., Doronzo, D. M., & Sarocchi, D. (2014). Pyroclastic density currents: State of the art and perspectives. *Journal of Volcanology and Geothermal Research*, *283*, 36–65. https://doi.org/10.1016/j.jvolgeores.2014.06.014

Trolese, M., Cerminara, M., Esposti Ongaro, T., & Giordano, G. (2019). The footprint of column collapse regimes on pyroclastic flow temperatures and plume heights. *Nature Communications*, *10*, 2476. https://doi.org/10.1038/s41467-019-10337-3

Trolese, M., Giordano, G., Cifelli, F., Winkler, A., & Mattei, M. (2017). Forced transport of thermal energy in magmatic and phreatomagmatic large volume ignimbrites: Paleomagnetic evidence from the Colli Albani volcano, Italy. *Earth and Planetary Science Letters*, *478*, 179–191. https://doi.org/10.1016/j.epsl.2017.09.004

Valentine, G. A. (2020). Initiation of dilute and concentrated pyroclastic currents from collapsing mixtures and origin of their proximal deposits. *Bulletin of Volcanology*, *82*, 20. https://doi.org/10.1007/s00445-020-1366-x

Valentine, G. A., & Fisher, R. V. (2000). Pyroclastic surges and blasts. In H. Sigurdsson (Ed.), *Encyclopedia of Volcanoes* (pp. 571–580). San Diego, Academic Press.

Wohletz, K. H. (1998). Pyroclastic surges and two-phase compressible flows. In A. Freundt, M. Rosi (Eds.), *From Magma to Tephra* (pp. 247–312). New York, Elsevier.

Wohletz, K. H., & Sheridan, M. F. (1979). A model of pyroclastic surge. *Geological Society of America Special Paper*, *180*, 177–194.

References From the Supporting Information

Benjamin, T. B. (1968). Gravity currents and related phenomena. *Journal of Fluid Mechanics*, *31*, 209–248. https://doi.org/10.1017/S0022112068000133

Druitt, T. H., Avard, G., Bruni, G., Lettieri, P., & Maez, F. (2007). Gas retention in fine-grained pyroclastic flow materials at high temperatures. *Bulletin of Volcanology*, *69*, 881–901. https://doi.org/10.1007/s00445-007-0116-7

Haar, L., Gallagher, J. S., & Kell, G. S. (1984). *NBS/NRC Steam Tables: Thermodynamic and Transport Properties and Computer Program for Vapor and Liquid States of Water in SI Units* (320 p), Washington, D.C., Hemisphere Publishing.

Huppert, H. E., & Simpson, J. E. (1980). The slumping of gravity currents. *Journal of Fluid Mechanics, 99*, 785–799. https://doi.org/10.1017/S0022112080000894

Rogers, R. R., & Yau, M. K. (1989). *A Short Course in Cloud Physics* (235 p). New York, Pergamon Press.

Self, S., & Sparks, R. S. J. (1978). Characteristics of widespread pyroclastic deposits formed by the interaction of silicic magma and water. *Bulletin of Volcanology*, *41*, 196–212. https://doi.org/10.1007/BF02597223

Shimizu, H. A., Koyaguchi, T., & Suzuki, Y. J. (2017). A numerical shallow-water model for gravity currents for a wide range of density differences. *Progress in Earth and Planetary Science, 4*, 8. https://doi.org/10.1186/s40645-017-0120-2

Shimizu, H. A., Koyaguchi, T., Suzuki, Y. J., Brosch, E., Lube, G., & Cerminara, M. (2021). Validation of a two-layer depth-averaged model by comparison with an experimental dilute stratified pyroclastic density current. *Bulletin of Volcanology*, *83*, 73. https://doi.org/10.1007/s00445-021-01493-w

Sparks, R. S. J., Bursik, M. I., Carey, S. N., Gilbert, J. S., Glaze, L. S., Sigurdsson, H., & Woods, A. W. (1997). *Volcanic Plumes* (590 p). Chichester, John Wiley.

Toro, E. F. (2001). *Shock-Capturing Methods for Free-Surface Shallow Flows* (309 p). Chichester, Wiley.

Ungarish, M. (2007). A shallow-water model for high-Reynolds-number gravity currents for a wide range of density differences and fractional depths. *Journal of Fluid Mechanics, 579*, 373–382. https://doi.org/10.1017/S0022112007005484

Ungarish, M. (2020). *Gravity Currents and Intrusions: Analysis and Prediction* (786 p). Singapore, World Scientific.

Woods, A. W. (1993). Moist convection and the injection of volcanic ash into the atmosphere. *Journal of Geophysical Research: Solid Earth*, *98*, 17627–17636. https://doi.org/10.1029/93JB00718

Geophysical Research Letters

Supporting Information for

Dynamics and Deposits of Pyroclastic Density Currents in Magmatic and Phreatomagmatic Eruptions Revealed by a Two-Layer Depth-Averaged Model

Hiroyuki A. Shimizu[1,2], Takehiro Koyaguchi[3], and Yujiro J. Suzuki[3]

[1]Sabo & Landslide Technical Center, Tokyo, Japan.

[2]National Research Institute for Earth Science and Disaster Resilience, Ibaraki, Japan.

[3]Earthquake Research Institute, The University of Tokyo, Tokyo, Japan.

Corresponding author: Hiroyuki A. Shimizu (shimizu@stc.or.jp)

Contents of this file

Text S1 to S3

Additional Supporting Information (Files uploaded separately)

Captions for Supporting Movies S1 to S2

Introduction

In this supporting information, we provide the details of a two-layer model for pyroclastic density currents (PDCs) in magmatic and phreatomagmatic eruptions (Section S1), summarize the results of sensitivity analysis for parameters other than the mass fraction of external water at the source (Section S2), and summarize the notations of variables shown in this paper (Section S3). We also provide the captions for the Supporting Movies S1 and S2 for phreatomagmatic and magmatic eruptions, respectively.

S1. Details of two-layer model for pyroclastic density currents in magmatic and phreatomagmatic eruptions

This section provides the details of the present two-layer depth-averaged model for large-scale PDCs in magmatic and phreatomagmatic eruptions. This model is developed by combining a previous two-layer model for large-scale PDCs in magmatic eruptions (Shimizu et al., 2019) with a thermodynamical model for magmatic and phreatomagmatic eruptions (i.e., the thermal energy conservation for mixing of magma, external water, and ambient air in the collapsing eruption column; Koyaguchi & Woods, 1996). In the present model, an eruption column produced from the volcanic vent radially collapses to generate a dilute current with low particle volume fractions of $\lesssim 10^{-3}$ from the column edge (i.e., the distance from the center of column $r = r_0$) at a constant mass flow rate $\dot{M}_0$ during time $t > 0$ (see Figure 1 in the main text; cf. Shimizu et al., 2019). The dilute current radially spreads on the flat ground surface and can generate a dense basal current with a high particle volume fraction of ~ 0.5 through particle settling; i.e., a two-layer PDC can be generated. A deposit progressively aggrades upward from the bottom of the dense or dilute current. Shimizu et al. (2019) assumed that the source collapsing eruption column and the resulting dilute current consist of magma (i.e., volcanic particles and volcanic gas (water vapor)) and entrained ambient air, whereas this paper considers that they consist of external water (e.g., groundwater, lakes, and oceans) as well as magma and entrained air. The basic equations and source conditions of the present two-layer PDC model are shown below.

S1.1 Basic equations

The basic equations of the dilute current are modified from Shimizu et al. (2019), whereas those of the dense current and deposits are the same as Shimizu et al. (2019). The present dilute current can contain liquid water as well as solid particles, air, and water vapor at low temperatures < 373 K (i.e., 100ºC). To obtain the spatiotemporal variation of the mass fraction of liquid water in the dilute current, the condensation rate of water vapor and the resulting latent heat are considered in the equation system on the basis of moist eruption column models (Woods, 1993; Koyaguchi & Woods, 1996).

S1.1.1 Dilute current

The dilute current is modeled as a highly turbulent suspension current consisting of solid particles, water vapor, liquid water, and entrained ambient air. The basic equations of the radially spreading dilute current with thickness $h(r,t)$, velocity $u(r,t)$, mass density $\rho(r,t)$, solid particle mass fraction $n_{\mathrm{s}}(r,t)$, water vapor mass fraction $n_{\mathrm{v}}(r,t)$, liquid water mass fraction $n_{\mathrm{w}}(r,t)$, air mass fraction $n_{\mathrm{a}}(r,t)$, temperature $T(r,t)$, and specific heat at constant pressure $C_{\mathrm{p}}(r,t)$ are as follows.

Conservation of bulk mass:

$$\frac{\partial}{\partial t}(\rho h) + \frac{1}{r}\frac{\partial}{\partial r}(\rho u h r) = \rho_{\mathrm{a}} E|u| - (n_{\mathrm{s}} + n_{\mathrm{w}})\rho W_{\mathrm{s}}, \qquad \text{(S1)}$$

Conservation of entrained air mass:

$$\frac{\partial}{\partial t}(n_{\mathrm{a}}\rho h) + \frac{1}{r}\frac{\partial}{\partial r}(n_{\mathrm{a}}\rho u h r) = \rho_{\mathrm{a}} E|u|, \qquad \text{(S2)}$$

Conservation of solid particle mass:

$$\frac{\partial}{\partial t}(n_{\mathrm{s}}\rho h)+\frac{1}{r}\frac{\partial}{\partial r}(n_{\mathrm{s}}\rho uhr)=-n_{\mathrm{s}}\rho W_{\mathrm{s}}, \tag{S3}$$

Conservation of liquid water mass:

$$\frac{\partial}{\partial t}(n_{\mathrm{w}}\rho h)+\frac{1}{r}\frac{\partial}{\partial r}(n_{\mathrm{w}}\rho uhr)=c-n_{\mathrm{w}}\rho W_{\mathrm{s}}, \tag{S4}$$

Conservation of bulk momentum:

$$\begin{aligned}\frac{\partial}{\partial t}(\rho uh)+\frac{1}{r}\frac{\partial}{\partial r}(\rho u^2hr)+\frac{\partial}{\partial r}\left(\frac{\rho-\rho_{\mathrm{a}}}{2}gh^2\right)\\ =-(\rho-\rho_{\mathrm{a}})gh\frac{\partial z_{\mathrm{c}}}{\partial r}-(n_{\mathrm{s}}+n_{\mathrm{w}})\rho uW_{\mathrm{s}}\\ -\rho C_{\mathrm{dc}}(u-u_{\mathrm{H}})|u-u_{\mathrm{H}}|,\end{aligned} \tag{S5}$$

Conservation of bulk thermal energy:

$$\begin{aligned}\frac{\partial}{\partial t}(\rho C_{\mathrm{p}}Th)+\frac{1}{r}\frac{\partial}{\partial r}(\rho C_{\mathrm{p}}Tuhr)\\ =\rho_{\mathrm{a}}E|u|\left(C_{\mathrm{pa}}T_{\mathrm{a}}+\frac{u^2}{2}+\frac{gh}{2}\right)\\ -\rho W_{\mathrm{s}}\left((n_{\mathrm{s}}C_{\mathrm{s}}+n_{\mathrm{w}}C_{\mathrm{pw}})T-(n_{\mathrm{s}}+n_{\mathrm{w}})\frac{gh}{2}\right)+cL,\end{aligned} \tag{S6}$$

Equation of state:

$$\frac{1}{\rho}=\frac{n_{\mathrm{s}}}{\rho_{\mathrm{s}}}+\frac{n_{\mathrm{w}}}{\rho_{\mathrm{w}}}+\frac{T}{p}(n_{\mathrm{a}}R_{\mathrm{a}}+n_{\mathrm{v}}R_{\mathrm{v}}), \tag{S7}$$

where ρ_{a} is the density of ambient air, E is the entrainment coefficient (see Eq. (A.1) of Shimizu et al., 2019), W_{s} is the mean settling speed of solid particles (with liquid water) at the bottom of the dilute current, c is the condensation rate of water vapor, g is the gravitational acceleration, z_{c} is the height of the basal contact, C_{dc} is the basal-drag coefficient of the dilute current, u_{H} is the velocity of the dense basal current, C_{pa} is the specific heat of air at constant pressure, T_{a} is the temperature of ambient air, C_{s} is the specific heat of solid particles, C_{pw} is the specific heat of liquid water at constant pressure, L ($\equiv 2.5\times10^6-(C_{\mathrm{pw}}-C_{\mathrm{pv}})(T-273)$) is the latent heat (Rogers & Yau, 1989), C_{pv} is the specific heat of water vapor at constant pressure, ρ_{s} is the density of solid particles, ρ_{w} is the density of liquid water, R_{a} is the gas constant of air, and R_{v} is the gas constant of water vapor. The pressure of the dilute current (p) is approximated as the atmospheric pressure ($\rho_{\mathrm{a}}R_{\mathrm{a}}T_{\mathrm{a}}$) in Eq. (S7). The mass fractions satisfy the condition of $n_{\mathrm{s}}+n_{\mathrm{w}}+n_{\mathrm{v}}+n_{\mathrm{a}}=1$. The specific heat of the dilute current at constant pressure is given by $C_{\mathrm{p}}=n_{\mathrm{s}}C_{\mathrm{s}}+n_{\mathrm{w}}C_{\mathrm{pw}}+n_{\mathrm{a}}C_{\mathrm{pa}}+n_{\mathrm{v}}C_{\mathrm{pv}}$.

The condensation rate c depends on the saturation temperature of water ($T_{\mathrm{sat}}(r,t)$). The saturation temperature is obtained from the condition of

$$p_{\mathrm{sat}}(T_{\mathrm{sat}}) = p_{\mathrm{v}}(n_{\mathrm{v}}, n_{\mathrm{a}}), \tag{S8}$$

where p_{sat} is the saturation pressure of water (Haar et al., 1984; Rogers & Yau, 1989):

$$p_{\mathrm{sat}}(T_{\mathrm{sat}}) = 2.53 \times 10^{11}\big(1 - 0.002(T_{\mathrm{sat}} - 273)\big) \exp\left(-\frac{5.42 \times 10^{3}}{T_{\mathrm{sat}}}\right), \tag{S9}$$

and p_{v} is the partial pressure of water vapor:

$$p_{\mathrm{v}}(n_{\mathrm{v}}, n_{\mathrm{a}}) = \frac{n_{\mathrm{v}} R_{\mathrm{v}}}{n_{\mathrm{v}} R_{\mathrm{v}} + n_{\mathrm{a}} R_{\mathrm{a}}} p. \tag{S10}$$

The condensation rate c is obtained from the mass conservation of liquid water (Eq. (S4)) when all the water vaporizes (i.e., total vaporization: $T > T_{\mathrm{sat}}$, $n_{\mathrm{w}} = 0$, and $n_{\mathrm{v}} > 0$) or when no water vaporizes (i.e., zero vaporization: $n_{\mathrm{w}} > 0$ and $n_{\mathrm{v}} = 0$). When water vapor and liquid water coexist (i.e., partial vaporization: $T = T_{\mathrm{sat}}$, $n_{\mathrm{w}} > 0$, and $n_{\mathrm{v}} > 0$), the condensation rate c, temperature T, and water vapor mass fraction n_{v} (or liquid water mass fraction n_{w}) are obtained from Eqs. (S4), (S6), and (S8)–(S10).

For simplicity, all of the liquid water in the dilute current is assumed to cover the surface of particles (i.e., the presence of water droplets in the current is assumed negligible) and not to generate the aggregation of particles, although these effects can change the settling rate of particles and liquid water at the bottom of the dilute current (i.e., $(n_{\mathrm{s}} + n_{\mathrm{w}})\rho W_{\mathrm{s}}$). In our representative simulations shown in the main text, W_{s} is modeled by the terminal velocity for the mean particle diameter of $0.1\ \mathrm{mm}$ ($W_{\mathrm{s}} = 0.5\ \mathrm{m\ s^{-1}}$; see Eq. (12) of Shimizu et al., 2021). Our model also assumes the ambient air to have no relative humidity. The evaluation of these effects awaits further study.

To describe the realistic dynamics of the dilute current, a dynamical balance between the buoyancy pressure driving the flow front ($\sim(\rho_{\mathrm{N}} - \rho_{\mathrm{a}})gh_{\mathrm{N}}$) and the resistance pressure caused by the acceleration of the ambient air at the front ($\sim\rho_{\mathrm{a}} u_{\mathrm{N}}^2$):

$$\frac{\mathrm{d}r_{\mathrm{N}}}{\mathrm{d}t} = u_{\mathrm{N}} = F_{\mathrm{N}} \sqrt{\frac{\rho_{\mathrm{N}} - \rho_{\mathrm{a}}}{\rho_{\mathrm{a}}} g h_{\mathrm{N}}} \qquad \text{at} \quad r = r_{\mathrm{N}}(t) \tag{S11}$$

is taken into account (Ungarish, 2007; Shimizu et al., 2017, 2019). Here, the subscript N denotes the front and F_{N} is a non-dimensional parameter similar to the Froude number ($\sqrt{2}$; Benjamin, 1968; Shimizu et al., 2021). Although F_{N} is traditionally called the frontal "Froude number" by many previous studies on gravity currents (e.g., Huppert & Simpson, 1980; Ungarish, 2020), it is not exactly the Froude number ($Fr \equiv u/\sqrt{\frac{\rho-\rho_{\mathrm{a}}}{\rho} gh}$; cf. Toro, 2001).

S1.1.2 Dense current and deposits

The dense basal current is modeled as a homogeneous fluidized granular current consisting of solid particles and gas (Shimizu et al., 2019). The basic equations of the radially spreading dense current with thickness $h_{\mathrm{H}}(r,t)$ and velocity $u_{\mathrm{H}}(r,t)$ are as follows.
Conservation of solid particle mass:

$$\frac{\partial h_{\mathrm{H}}}{\partial t}+\frac{1}{r}\frac{\partial}{\partial r}(u_{\mathrm{H}}h_{\mathrm{H}}r)=\frac{\phi_{\mathrm{s}}}{\phi_{\mathrm{sH}}}W_{\mathrm{s}}-\frac{\phi_{\mathrm{sD}}}{\phi_{\mathrm{sH}}}D, \tag{S12}$$

Conservation of solid particle momentum:

$$\begin{aligned}\frac{\partial}{\partial t}(u_{\mathrm{H}}h_{\mathrm{H}})+\frac{1}{r}\frac{\partial}{\partial r}\left(u_{\mathrm{H}}^{2}h_{\mathrm{H}}r\right)+\frac{\partial}{\partial r}\left(\frac{1}{2}\frac{\rho_{\mathrm{H}}-\rho_{\mathrm{a}}}{\rho_{\mathrm{H}}}gh_{\mathrm{H}}^{2}\right)\\ =-\frac{\rho_{\mathrm{H}}-\rho_{\mathrm{a}}}{\rho_{\mathrm{H}}}gh_{\mathrm{H}}\frac{\partial z_{\mathrm{b}}}{\partial r}-\frac{h_{\mathrm{H}}}{\rho_{\mathrm{H}}}\frac{\partial}{\partial r}\left((\rho-\rho_{\mathrm{a}})gh\right)\\ +\frac{\phi_{\mathrm{s}}}{\phi_{\mathrm{sH}}}uW_{\mathrm{s}}-\frac{\phi_{\mathrm{sD}}}{\phi_{\mathrm{sH}}}u_{\mathrm{H}}D\\ +\frac{\rho}{\rho_{\mathrm{H}}}C_{\mathrm{dc}}(u-u_{\mathrm{H}})|u-u_{\mathrm{H}}|-C_{\mathrm{db}}u_{\mathrm{H}}|u_{\mathrm{H}}|,\end{aligned} \tag{S13}$$

where the subscript H denotes the high particle concentration (i.e., dense) current, ϕ_{s} ($\equiv n_{\mathrm{s}}\rho/\rho_{\mathrm{s}}$) is the volume fraction of solid particles in the upper dilute current, ϕ_{sH} is the volume fraction of solid particles in the dense current, ϕ_{sD} is the volume fraction of solid particles in the deposits, D is the mean deposition speed at the bottom of the dense current, z_{b} is the height of the contact between the dense current and the deposits, and C_{db} is the basal-drag coefficient of the dense current. The dense current is assumed to have a constant bulk density $\rho_{\mathrm{H}}=\phi_{\mathrm{sH}}\rho_{\mathrm{s}}+(1-\phi_{\mathrm{sH}})\rho_{\mathrm{gH}}$, where ρ_{gH} ($=p/(R_{\mathrm{a}}T_0)$) is the density of the gas phase in the dense current, and T_0 is the source temperature of the upper dilute current (see the next subsection). Note that the effect of liquid water coating the surfaces of particles settling from the upper dilute current is assumed negligible. In our representative simulations shown in the main text, D is modeled by the hindered settling for poorly sorted materials (i.e., $D/W_{\mathrm{s}}=1.22\times10^{-3}$; see Eqs. (11)–(13) of Shimizu et al., 2021).

The deposits progressively aggrade upward from the bottom of the dense or dilute current (Shimizu et al., 2019). The aggradation rate of material in the deposits can be written as

$$\frac{\partial z_{\mathrm{b}}}{\partial t}=\begin{cases}D & (\text{Aggradation from dense current}),\\ \dfrac{\phi_{\mathrm{s}}}{\phi_{\mathrm{sD}}}W_{\mathrm{s}} & (\text{Aggradation from dilute current}).\end{cases} \tag{S14}$$

The aggradation for the dilute current occurs when the particle-settling rate at the bottom of the dilute current is smaller than the deposition rate of the dense current (i.e., the right-hand side of Eq. (S12) <0) at the position where the dense current is absent (i.e., $h_{\mathrm{H}}=0$). In the present model where no dense current is supplied directly from the source column, when the particle settling rate from the bottom of the dilute current at the source $r=r_0$ (i.e., $\phi_{\mathrm{s0}}W_{\mathrm{s}}$) is smaller than the deposition rate from the bottom of the dense current (i.e., $\phi_{\mathrm{sD}}D$), the dense current is absent throughout $r>r_0$.

S1.2 Source boundary conditions

The source conditions of the dilute current are given as follows. Hot fragmented magma with temperature T_{m} and water mass fraction w_{m} mixes with cold external water with temperature T_{w} and is ejected from the vent; this study considers a wide range of mass fractions of external water in the mixture of magma and external water ($w_{\mathrm{mw}}=0$– 0.6). The ejected material mixes with ambient air with temperature T_{a} to form a collapsing column, which in turn forms a dilute current from the column edge. When these variables and the mass fractions of magma, external water, and entrained ambient air (m ($\equiv 1 - w - a$), w ($\equiv w_{\mathrm{mw}}(1 - a)$), and a, respectively) are given, some source boundary conditions for the dilute current at the column edge (i.e., source mass fractions of solid particles n_{s0}, liquid water n_{w0}, water vapor n_{v0}, and entrained air n_{a0}) are estimated as

$$n_{\mathrm{s0}} = (1 - w_{\mathrm{m}})m, \tag{S12}$$

$$n_{\mathrm{w0}} = (1 - w_{\mathrm{v}})w, \tag{S13}$$

$$n_{\mathrm{v0}} = w_{\mathrm{m}}m + w_{\mathrm{v}}w, \tag{S14}$$

$$n_{\mathrm{a0}} = a, \tag{S15}$$

where w_{v} is the mass fraction of the external water that vaporizes, and the relative humidity is assumed to be zero. The source temperature T_0 and w_{v} are estimated by the thermal energy conservation for mixing of magma, external water, and air at atmospheric pressure (Koyaguchi & Woods, 1996), depending on three qualitatively different styles of mixing as follows.
Total vaporization ($T_0 > T_{\mathrm{sat0}}$ and $w_{\mathrm{v}} = 1$):

$$\begin{aligned} & m\{(1 - w_{\mathrm{m}})C_{\mathrm{s}} + w_{\mathrm{m}}C_{\mathrm{pv}}\}(T_0 - T_{\mathrm{m}}) \\ & +w\{C_{\mathrm{pw}}(T_{\mathrm{sat0}} - T_{\mathrm{w}}) + L(T_{\mathrm{sat0}}) + C_{\mathrm{pv}}(T_0 - T_{\mathrm{sat0}})\} \\ & +aC_{\mathrm{pa}}(T_0 - T_{\mathrm{a}}) = 0, \end{aligned} \tag{S16}$$

Partial vaporization ($T_0 = T_{\mathrm{sat0}}$ and $w_{\mathrm{v,min}} < w_{\mathrm{v}} < 1$):

$$\begin{aligned} & m\{(1 - w_{\mathrm{m}})C_{\mathrm{s}} + w_{\mathrm{m}}C_{\mathrm{pv}}\}(T_{\mathrm{sat0}} - T_{\mathrm{m}}) \\ & +w\{C_{\mathrm{pw}}(T_{\mathrm{sat0}} - T_{\mathrm{w}}) + w_{\mathrm{v}}L(T_{\mathrm{sat0}})\} \\ & +aC_{\mathrm{pa}}(T_{\mathrm{sat0}} - T_{\mathrm{a}}) = 0, \end{aligned} \tag{S17}$$

Zero vaporization ($T_0 < T_{\mathrm{sat0}}$ and $w_{\mathrm{v}} = w_{\mathrm{v,min}}$):

$$\begin{aligned} & m[(1 - w_{\mathrm{m}})C_{\mathrm{s}} + w_{\mathrm{m}}\{C_{\mathrm{pv}}(T_{\mathrm{sat0}} - T_{\mathrm{m}}) - L(T_{\mathrm{sat0}}) + C_{\mathrm{pw}}(T_0 - T_{\mathrm{sat0}})\}] \\ & +wC_{\mathrm{pw}}(T_0 - T_{\mathrm{w}}) \\ & +aC_{\mathrm{pa}}(T_0 - T_{\mathrm{a}}) = 0, \end{aligned} \tag{S18}$$

where the saturation temperature at the column edge (T_{sat0}) is given by Eqs. (S8)–(S10), the minimum value of w_{v} ($w_{\mathrm{v,min}}$) is given by $-w_{\mathrm{m}}m/w$, and the latent heat ($L(T_{\mathrm{sat0}})$) is given by $2.5 \times 10^6 - (C_{\mathrm{pw}} - C_{\mathrm{pv}})(T_{\mathrm{sat0}} - 273)$ (Rogers & Yau, 1989). Given the mass densities of solid particles and liquid water (ρ_{s} and ρ_{w}, respectively), the bulk mass density of the dilute current at the column edge (ρ_0) is determined by the equation of state (Eq. (S7)).

The other source conditions for the dilute current at the column edge (i.e., the thickness h_0, velocity u_0, and the radius of the collapsing column r_0) are obtained from the mass flow rate at the column edge ($\dot{M}_0 \equiv 2\pi r_0 \rho_0 u_0 h_0$), the Richardson number at the column edge ($Ri_0 \equiv (\rho_0 - \rho_{\mathrm{a}})g\mathrm{h}_0/(\rho_0 u_0^2)$), and the aspect ratio ($a_0 \equiv h_0/r_0$) (Shimizu et al., 2019):

$$h_0 = \left\{ \left(\frac{a_0 \dot{M}_0}{2\pi\rho_0} \right)^2 \Big/ \left(\frac{\rho_0 - \rho_\mathrm{a}}{\rho_0} g / Ri_0 \right) \right\}^{1/5} , \tag{S19}$$

$$u_0 = \left\{ \frac{a_0 \dot{M}_0}{2\pi\rho_0} \left(\frac{\rho_0 - \rho_\mathrm{a}}{\rho_0} g / Ri_0 \right)^2 \right\}^{1/5} , \tag{S20}$$

$$r_0 = \frac{1}{a_0} \left\{ \left(\frac{a_0 \dot{M}_0}{2\pi\rho_0} \right)^2 \Big/ \left(\frac{\rho_0 - \rho_\mathrm{a}}{\rho_0} g / Ri_0 \right) \right\}^{1/5} . \tag{S21}$$

Here, $\dot{M}_0$ is directly related to the magma discharge rate $\dot{M}_\mathrm{m}$ (i.e., $\dot{M}_0 = \dot{M}_\mathrm{m}/m$). Although whether the eruption column totally/partially collapses or not depend on the values of the parameters such as $\dot{M}_\mathrm{m}$, w_mw (Koyaguchi & Woods, 1996), and n_a0 (Trolese et al., 2019), we assume the total collapse regardless of these parameters for simplicity.

The values of the parameters are summarized in Tables S1 and S2 (w_mw varying every 0.05 from 0 to 0.6); Series 1 is the numerical simulations shown in the main text, where the numerical simulations with $w_\mathrm{mw} = 0.07$ and 0.38 were also performed to confirm the absence of dense currents.

Table S1. Common input parameters and constants for simulations.

Variable	Value [Unit]	Meaning
C_{db}	10^{-4}	Basal-drag coefficient of dense current
C_{dc}	10^{-4}	Basal-drag coefficient of dilute current
C_{pa}	1004 [J kg^{-1} K^{-1}]	Specific heat of air at constant pressure
C_{pv}	1810 [J kg^{-1} K^{-1}]	Specific heat of water vapor at constant pressure
C_{pw}	4187 [J kg^{-1} K^{-1}]	Specific heat of liquid water at constant pressure
C_{s}	1100 [J kg^{-1} K^{-1}]	Specific heat of solid particles
F_{N}	$\sqrt{2}$	Non-dimensional parameter for the frontal dynamical balance
g	9.81 [m s^{-2}]	Gravitational acceleration
p	1.013×10^{5} [Pa]	Pressure
R_{a}	287 [J kg^{-1} K^{-1}]	Gas constant of air
R_{v}	462 [J kg^{-1} K^{-1}]	Gas constant of water vapor
T_{a}	273 [K]	Temperature of ambient air
T_{w}	273 [K]	Temperature of external water
ρ_{s}	2600 [kg m^{-3}]	Mass density of solid particles
ρ_{w}	1000 [kg m^{-3}]	Mass density of liquid water

Table S2. Summary of the input parameters of all simulation series.

Series	w_{mw}	w_{m}	T_{m} [K]	n_{a0}	$\dot{M}_{\mathrm{m}}$ [kg s^{-1}]	Ri_0	a_0	W_{s} [m s^{-1}]	D/W_{s}
1	0– 0.6	0.03	1000	0.07	10^{9}	1	0.2	0.5	1.22×10^{-3}
2	0– 0.6	0.06	1000	0.07	10^{9}	1	0.2	0.5	1.22×10^{-3}
3	0– 0.6	0.03	800	0.07	10^{9}	1	0.2	0.5	1.22×10^{-3}
4	0– 0.6	0.03	1200	0.07	10^{9}	1	0.2	0.5	1.22×10^{-3}
5	0– 0.6	0.03	1000	0.01	10^{9}	1	0.2	0.5	1.22×10^{-3}
6	0– 0.6	0.03	1000	0.15	10^9	1	0.2	0.5	1.22×10^{-3}
7	0– 0.6	0.03	1000	0.07	10^{7}	1	0.2	0.5	1.22×10^{-3}
8	0– 0.6	0.03	1000	0.07	10^{11}	1	0.2	0.5	1.22×10^{-3}
9	0– 0.6	0.03	1000	0.07	10^{9}	0.1	0.2	0.5	1.22×10^{-3}
10	0– 0.6	0.03	1000	0.07	10^{9}	1	0.1	0.5	1.22×10^{-3}
11	0– 0.6	0.03	1000	0.07	10^{9}	1	0.5	0.5	1.22×10^{-3}
12	0– 0.6	0.03	1000	0.07	10^{9}	1	0.2	0.005	1.22×10^{-3}
13	0– 0.6	0.03	1000	0.07	10^{9}	1	0.2	5	1.22×10^{-3}
14	0– 0.6	0.03	1000	0.07	10^{9}	1	0.2	0.5	1×10^{-3}
15	0– 0.6	0.03	1000	0.07	10^{9}	1	0.2	0.5	2×10^{-3}

S2. Summary of sensitivity analysis results for parameters other than w_{mw}

This section summarizes the results of sensitivity analysis to investigate the effects of the variations in parameters other than the mass fraction of external water at the source (w_{mw}). The conclusion in the main text is derived on the basis of the results of Series 1 in Table S2; the datasets for these results are available in Zenodo (Shimizu, 2023; doi: 10.5281/zenodo.7928713). We performed additional numerical simulations of the two-layer PDC model for the mass fraction of water in the magma $w_{\mathrm{m}} = 0.03$– 0.06, the magma temperature $T_{\mathrm{m}} = 800$– $1200\ \mathrm{K}$, the mass fraction of air in the dilute current at the column edge $n_{\mathrm{a0}} = 0.01$– 0.15, the magma discharge rate $\dot{M}_{\mathrm{m}} = 10^{7}$– $10^{11}\ \ \mathrm{kg\ s^{-1}}$, the Richardson number of the dilute current at the column edge $Ri_{0} = 0.1$– 1, the aspect ratio of the thickness of the dilute current at the column edge to the radius of the column $a_{0} = 0.1$– 0.5, the mean settling speed of particles at the bottom of the dilute current $W_{\mathrm{s}} = 0.005$– $5\ \mathrm{m\ s^{-1}}$, and the normalized mean deposition speed at the bottom of the dense basal current $D/W_{\mathrm{s}} = 1 \times 10^{-3}$– 2×10^{-3} (i.e., Series 2–15 in Table S2). The datasets for these results are made available on request.

Here, we show representative results to assess the effects of the above variations on our main conclusions: those are the increase in the run-out distance of dilute currents with w_{mw} and the tendency that the dense current is absent for intermediate values of w_{mw} (Figure S1). The results show that all the effects do not qualitatively change the conclusions, whereas some of them modify the conclusions in a quantitative sense. The run-out distance of dilute currents increases with the increase in w_{mw} for given w_{m}, T_{m}, n_{a0}, $\dot{M}_{\mathrm{m}}$, W_{s}, and D/W_{s}; it also increases with the decreases in T_{m} and W_{s} and the increase in $\dot{M}_{\mathrm{m}}$ (Figure S1). The tendency that the dense current is absent for intermediate values of w_{mw} remains valid regardless of w_{m}, T_{m}, n_{a0}, $\dot{M}_{\mathrm{m}}$, W_{s}, and D/W_{s} (Figure S1); the critical values of w_{mw} for the absence of dense currents, however, depend quantitatively on w_{m}, T_{m}, n_{a0}, and D/W_{s} (Figure S1a–c and f). This feature is explained by the fact that the volume fraction of solid particles in the dilute current at the column edge (ϕ_{s0}) is a convex downward function of w_{mw} for given parameters; the absence of dense currents is determined by the relative magnitude of D/W_{s} and ϕ_{s0} as mentioned in the main text, and ϕ_{s0} increases as w_{m}, T_{m}, and n_{a0} decrease (Figure S2).

Finally, we point out that the values of W_{s} and D/W_{s} are given independently of w_{mw} in this paper for simplicity. These values generally depend on w_{mw} (cf. Self & Sparks, 1978; Sparks et al., 1997; Druitt et al., 2007). The increase in w_{mw} can lead to the decrease in the mean particle diameter (i.e., the decrease in W_{s} and the increase in D/W_{s}) owing to enhanced fragmentation during dry phreatomagmatic eruptions (i.e., $n_{\mathrm{w0}} = 0$). During wet phreatomagmatic eruptions (i.e., $n_{\mathrm{w0}} > 0$), on the other hand, it can lead to the increase in the effective particle diameter (i.e., the increase in W_{s} and the decrease in D/W_{s}) owing to ash aggregation. The quantitative relationship of the sedimentation process in PDCs (i.e., W_{s} and D) with w_{mw} needs further clarification.

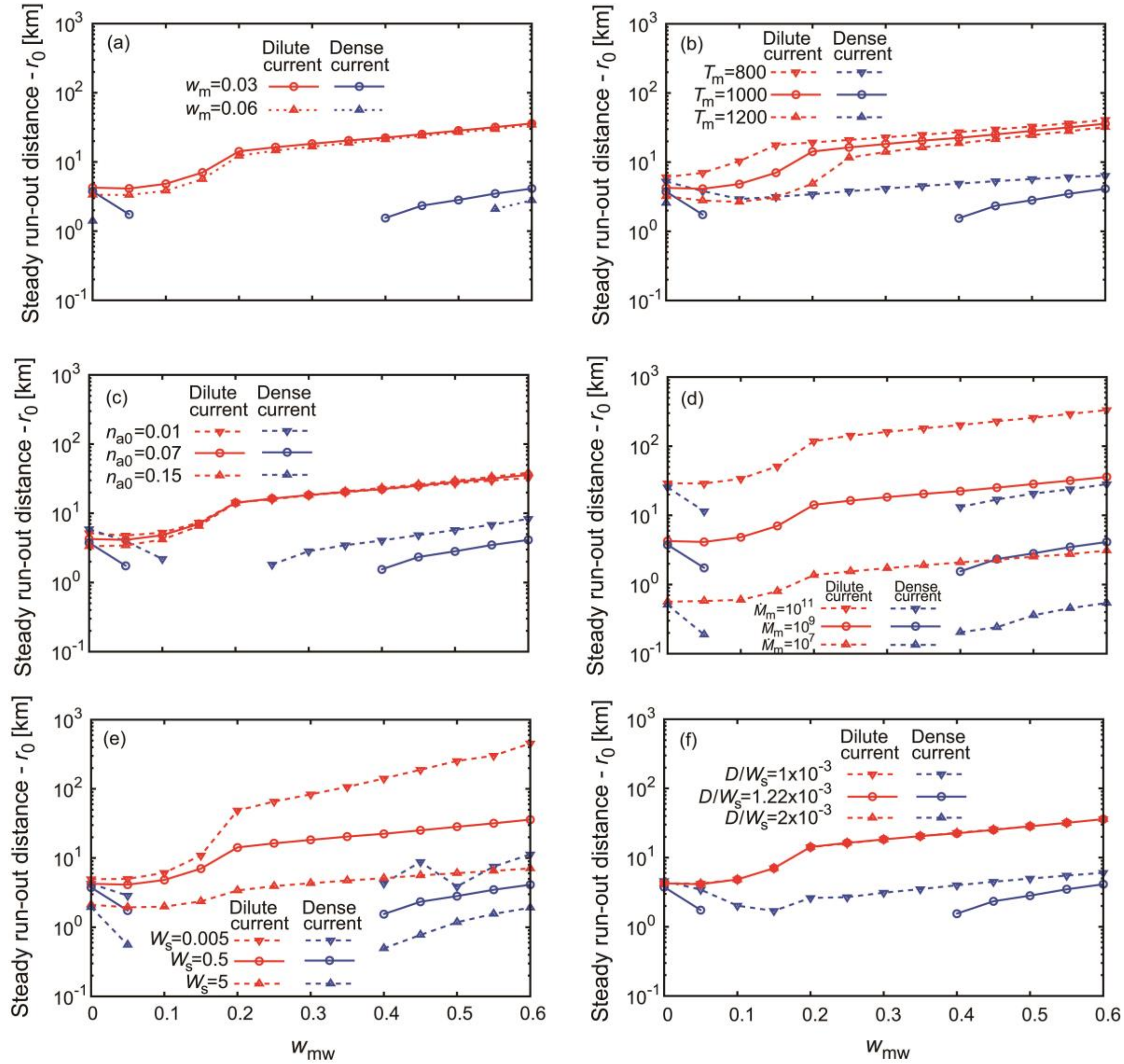

Figure S1. Numerical results of the differences of the steady run-out distances of two-layer PDCs from the column radius r_0 as a function of mass fraction of external water in the mixture of magma and external water w_{mw}. Red and blue curves indicate dilute and dense currents, respectively. (a) Effects of mass fraction of water in the magma $w_{\mathrm{m}} = 0.03$ (circles; Series 1) and 0.06 (triangles; Series 2) (b) Effects of magma temperature $T_{\mathrm{m}} = 1000$ (circles; Series 1), 800 (inverted triangles; Series 3), and 1200 K (triangles; Series 4). (c) Effects of mass fraction of air in dilute current at the column edge $n_{\mathrm{a0}} = 0.07$ (circles; Series 1), 0.01 (inverted triangles; Series 5), and 0.15 (triangles; Series 6). (d) Effects of magma discharge rate $\dot{M}_{\mathrm{m}} = 10^9$ (circles; Series 1), 10^7 (triangles; Series 7), and 10^{11} $\mathrm{kg\ s^{-1}}$ (inverted triangles; Series 8). (e) Effects of mean settling speed of particles at the bottom of dilute current $W_{\mathrm{s}} = 0.5$ (circles; Series 1), 0.005 (inverted triangles; Series 12), and 5 $\mathrm{m\ s^{-1}}$ (triangles; Series 13). (f) Effects of normalized mean deposition speed at the bottom of dense current $D/W_{\mathrm{s}} = 1.22 \times 10^{-3}$ (circles; Series 1), 1×10^{-3} (inverted triangles; Series 14), and 2×10^{-3} (triangles; Series 15).

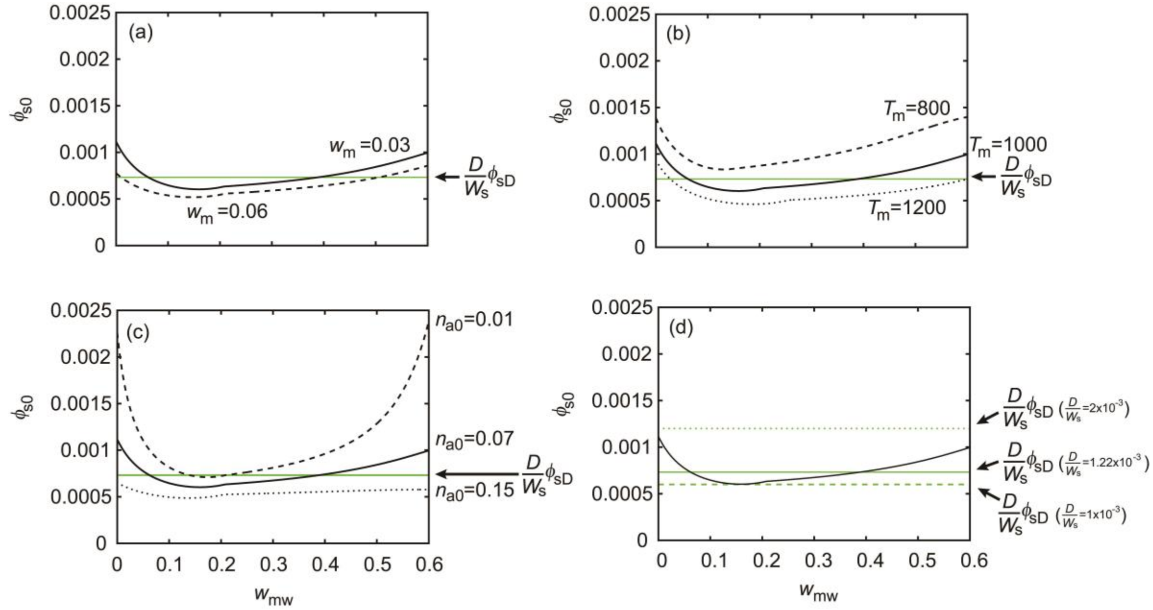

Figure S2. Relationships of the volume fraction of solid particles in the dilute current at the column edge ϕ_{s0} (black curves) to the mass fraction of external water in the mixture of magma and external water w_{mw}, compared with $\phi_{sD}D/W_s$ (green lines). (a) Effects of mass fraction of water in the magma $w_m = 0.03$ (black solid curve; Series 1) and 0.06 (black dashed curve; Series 2). (b) Effects of magma temperature $T_m = 1000$ (black solid curve; Series 1), 800 (black dashed curve; Series 3), and 1200 K (black dotted curve; Series 4). (c) Effects of mass fraction of air in dilute current at the column edge $n_{a0} = 0.07$ (black solid curve; Series 1), 0.01 (black dashed curve; Series 5), and 0.15 (black dotted curve; Series 6). (d) Effects of normalized mean deposition speed at the bottom of dense current $D/W_s = 1.22 \times 10^{-3}$ (green solid line; Series 1), 1×10^{-3} (green dashed line; Series 14), and 2×10^{-3} (green dotted line; Series 15).

S3. Summary of notations

a	Mass fraction of air in source mixture of magma, external water, and entrained air
a_0	Aspect ratio of h_0 to r_0
c	Condensation rate of water vapor in dilute current, $\mathrm{kg\ m^{-2}\ s^{-1}}$
C_d	Basal-drag coefficient
C_p	Specific heat (of dilute current) at constant pressure, $\mathrm{J\ kg^{-1}\ K^{-1}}$
C_s	Specific heat of solid particles, $\mathrm{J\ kg^{-1}\ K^{-1}}$
D	(Mean) deposition speed at bottom of dense current, $\mathrm{m\ s^{-1}}$
E	Entrainment coefficient
F_N	Non-dimensional parameter for frontal dynamical balance
Fr	Froude number
g	Gravitational acceleration, $\mathrm{m\ s^{-2}}$
h	Thickness of (dilute) current, m
L	Latent heat, $\mathrm{J\ kg^{-1}}$
m	Mass fraction of magma in source mixture of magma, external water, and entrained air
$\dot{M}$	Mass flow rate, $\mathrm{kg\ s^{-1}}$
n	Mass fraction
p	Pressure, Pa
r	Distance (i.e., radius) from volcanic vent, m
R	Gas constant, $\mathrm{J\ kg^{-1}\ K^{-1}}$
Ri	Richardson number of dilute current
t	Time, s
T	Temperature (of dilute current), K
u	Velocity component of (dilute) current in r direction, $\mathrm{m\ s^{-1}}$
w	Mass fraction of external water in source mixture of magma, external water, and entrained air
w_m	Mass fraction of water in magma
w_mw	Mass fraction of external water in mixture of magma and external water
w_v	Mass fraction of external water that vaporizes in source collapsing column
W_s	(Mean) settling speed of solid particles at bottom of dilute current, $\mathrm{m\ s^{-1}}$
z	Coordinate in vertical direction, m
ρ	Mass density, $\mathrm{kg\ m^{-3}}$
ϕ_s	Volume fraction of solid particles

Subscript

a	Ambient air
b	Upper surface of ground surface of deposit (i.e., base of (dense) current)
c	Upper surface of dense current (i.e., contact surface between dilute and dense currents)
D	Deposit
f	Upper surface of dilute current
g	Gas phase

H	Dense (i.e., high particle concentration) current
m	Magma
min	Minimum value
mw	Magma and external water
N	Front (i.e., nose) of dilute current
s	Solid particle
sat	Saturation
v	Water vapor
w	Liquid water
0	Edge of source collapsing eruption column

Movie S1. Representative numerical results of a two-layer PDC for phreatomagmatic eruption with $w_{\mathrm{mw}} = 0.3$ (see Tables S1 and S2 (Series 1) for the other parameters). The thickness profiles of the dilute current ($h(r,t)$; red), dense current ($h_{\mathrm{H}}(r,t)$; blue), and deposits ($z_{\mathrm{b}}(r,t)$; black) are shown.

Movie S2. Representative numerical results of a two-layer PDC for magmatic eruption with $w_{\mathrm{mw}} = 0$ (see Tables S1 and S2 (Series 1) for the other parameters). The thickness profiles of the dilute current ($h(r,t)$; red), dense current ($h_{\mathrm{H}}(r,t)$; blue), and deposits ($z_{\mathrm{b}}(r,t)$; black) are shown.